Materials Characterization xxx (xxxx) xxx

Contents lists available at ScienceDirect

Materials Characterization

journal homepage: www.elsevier.com/locate/matchar

Microstructural and micro-mechanical analysis of 14YWT nanostructured Ferritic alloy after varying thermo-mechanical processing paths into tubing

Cayla Harvey [a,*], Osman El Atwani [b], Hyosim Kim [b], Curt Lavender [c], Marie McCoy [c], Denis Sornin [d], John Lewandowski [e], Stuart A. Maloy [b], Siddhartha Pathak [f]

[a] Chemical and Materials Engineering, University of Nevada, Reno, NV 89557, USA
[b] Materials Science and Technology Division, Los Alamos National Laboratory, Los Alamos, NM, USA
[c] Pacific Northwest National Laboratory, Richland, WA, USA
[d] Université Paris-Saclay, CEA, Service de Recherches Métallurgiques Appliquées, 91191 Gif-sur-Yvette, France
[e] Department of Materials Science and Engineering, Case Western Reserve University, Cleveland, OH 44106, USA
[f] Department of Materials Science and Engineering, Iowa State University, Ames, IA 50011, USA

ARTICLE INFO

Keywords:
ODS
14YWT
Oxide particles
Micro-pillar

ABSTRACT

Microstructural analyses and micro-pillar compression were conducted on 14YWT nanostructured ferritic alloy (NFA) to compare different processing pathways: hydrostatic extrusion and Pilger processing with varying annealing temperatures into thin walled tubing, and after hot extrusion and cross-rolling into a plate. Hydrostatic extrusion at 815 °C resulted in the smallest grain sizes and highest yield strength of 1.20 GPa. Pilger processing with annealing at 800 °C had fine grained regions and bands of coarse grains, leading to a large variation in yield strength of 0.9–1.40 GPa. Higher annealing temperatures of 1200 °C after pilger processing significantly increased the grain size and lowered the yield strength to 1.01 GPa. These tubes showed a stronger ⟨111⟩ crystallographic texture in the normal direction and elongated grains in the extrusion direction. Characterization of the nano-oxides using TEM reveals more numerous, smaller oxides present in tubing processed at lower temperatures. This work shows NFA tubing after hydrostatic extrusion and pilger processing can lead to fine grained microstructures and texturing leading to higher yield strengths at lower annealing temperatures (*e.g.* 800 °C).

1. Introduction

Ferritic/martensitic oxide dispersion strengthened (ODS) steels with high chromium content (>9% Cr) for ferrite stabilization are considered for structural materials in Generation IV liquid metal fast reactors operating at elevated temperatures with increased irradiation damage [1–5]. These steels display higher radiation tolerance to void swelling than austenitic steels [4]. To further enhance their structural stability and strength, adding high densities of nanometer sized precipitates is of interest as they pin grain boundaries and dislocations and provide sinks for radiation produced defects [1,2,4]. Development of ODS steels has led to a variety of nanostructure ferritic alloys (NFAs), designed with a high density of Y-Ti-O nano-oxides (NOs). NFAs generally have ~12–16 wt% Cr, ~1–3 wt% W, and small quantities (<1 wt%) of Ti, Y and O [1,2,6,7]. The NOs remarkably act as vacancy and self-interstitial atom defect recombination centers while also trapping the radiation transmutation product helium into small bubbles at interfaces [4].

NFAs are targeted for application as fuel cladding, with extensive research being conducted to optimize the thermo-mechanical processing pathways that yield seamless tubing [8]. Current issues with NFAs include anisotropic textures resulting in variations in mechanical properties after hot consolidation and extrusion. This stems from the NOs and grains aligning in the deformation direction during recrystallization and grain growth [9]. The Zener pinning force of the NOs in the transverse direction creates the anisotropic textures and bi-modal or multi-modal grain distributions [10–14]. These bi-modal grain sizes can have some advantages as the larger grains enhance ductility and the smaller grains enhance strength [15,16]. The grain sizes result from the distribution of second phase particles. Also, one of the drawbacks is that the bi-modal grain sizes can result in inhomogeneous NO distribution within different sized grains. Previous studies on NFAs show the density of NOs in smaller grains is generally higher than in larger grains [17].

* Corresponding author.
E-mail addresses: caylaharvey@nevada.unr.edu (C. Harvey), pathak@iastate.edu (S. Pathak).

https://doi.org/10.1016/j.matchar.2020.110744
Received 17 August 2020; Received in revised form 30 October 2020; Accepted 2 November 2020
Available online 5 November 2020

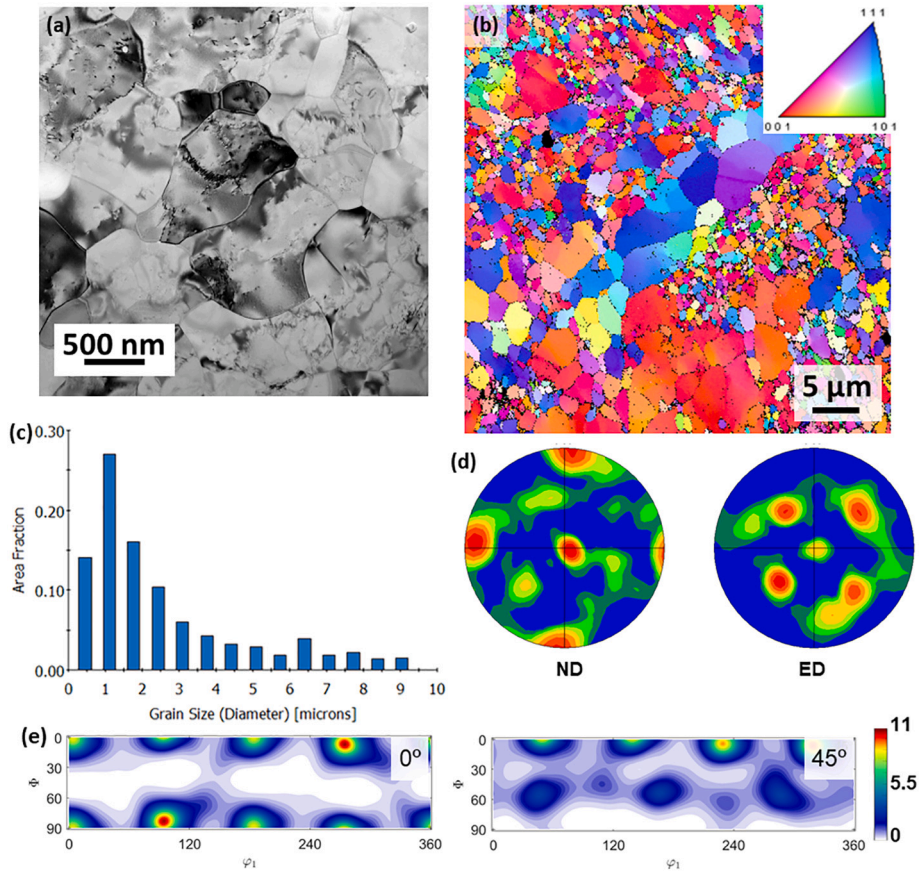

Fig. 1. Hot extruded at 850 °C and crossed rolled plate at 1000 °C (a) TEM image (b) EBSD generated IPF map (c) grain diameter distribution (d) Pole Figures in the ND and ED (e) ODF represented as sections through Euler space at constant φ2 values of 0° and 45°.

Overall, the variation in grain sizes has shown improved mechanical properties, although the different textures in extruded plates and tubing can significantly affect the yield strength and creep strength [1,4,18,19].

An additional issue that occurs during processing is the formation of cracks within plates after extrusion and cross-rolling, leading to brittle behavior. Hot extrusion of NFAs into cross-rolled plates show micro-cracks and radial through wall cracks [20]. These properties present challenges in the fabrication of NFAs with minimal defects. Processing methods generally incorporate heat treatments to reduce brittleness and soften the alloy. A current processing path of interest is hydrostatic extrusion that has been shown to process low ductility materials into net shape with less anisotropic properties. Aydogan et al. [21] investigated the differences between two processing methods, where hydrostatic extrusion with plane strain and shear deformation resulted in weaker textures with stronger α-001⟨110⟩ and γ-111<110> fibers, indicating that this processing path results in a more desirable isotropic texture. Pilger processing has also shown to produce a preferred texture in ODS steels with 9%Cr [22,23]. Multiple cold rolling steps to reduce the tube diameter and thickness with intermediate and final heat treatments reduced the amount of elongated grains, as well as improved creep and tensile strengths.

A direct comparison of different tubing processing paths on the resultant properties for NFAs has yet to be reported. We study a specific heat of NFA named 14YWT with a nominal composition of Fe-14Cr-3 W-0.4Ti-0.2Y(wt%), which has been extensively studied due to its high irradiation tolerance, strength, and toughness. Most investigations in literature have focused on the effect of irradiation on the microstructure [6,17,20] or tensile strength of extruded plates [24]. This current work aims to investigate the effect of hydrostatic extrusion and pilger processing methods with varying annealing temperatures (800 °C and 1200 °C) of a specific heat of 14YWT into thin-walled tubing, as well as (non-tubing) hot extruded plate processing path. Here, we determine the mechanical properties of the 14YWT alloys using micro-pillar compression testing, which will serve as a baseline for future work where similar testing will be conducted after ion-irradiation of the same material. Micro-pillar testing was chosen since these test volumes are complementary to the volumes of future ion-irradiation experiments, which are typically limited by the beam energy to depths of sub-µm to several µm [25].

This manuscript is organized as follows. We start with the electron backscatter diffraction (EBSD) and transmission electron microscopy (TEM) characterization of the 14YWT microstructure as well as the NOs. Results from micro-mechanical testing using *in-situ* micropillar compression experiments are discussed next. For each section the results are described in terms of the processing path and in order of decreasing final grain size in the microstructure after processing: hot extrusion followed by cross-rolling, pilger processing with annealing at 1200 °C, hydrostatic extrusion at 815 °C, and pilger processing with annealing at 800 °C.

2. Material and methods

The NFA 14YWT heat named FCRD NFA-1 was developed as part of the DOE Fuel Cycle Research and Development Program with a nominal composition of 14Cr-3 W-0.4Ti-0.21Y-Fe wt%, as a collaboration between Los Alamos National Laboratory, Oak Ridge National Laboratory and University of California, Santa Barbara. ATI Powder Metals Laboratory produced the precursor powder *via* gas atomization. To solutionize Y into the Fe matrix, Zoz, GmbH mechanically alloyed the powders with FeO additions (for added oxygen) for 40 h in an attritor

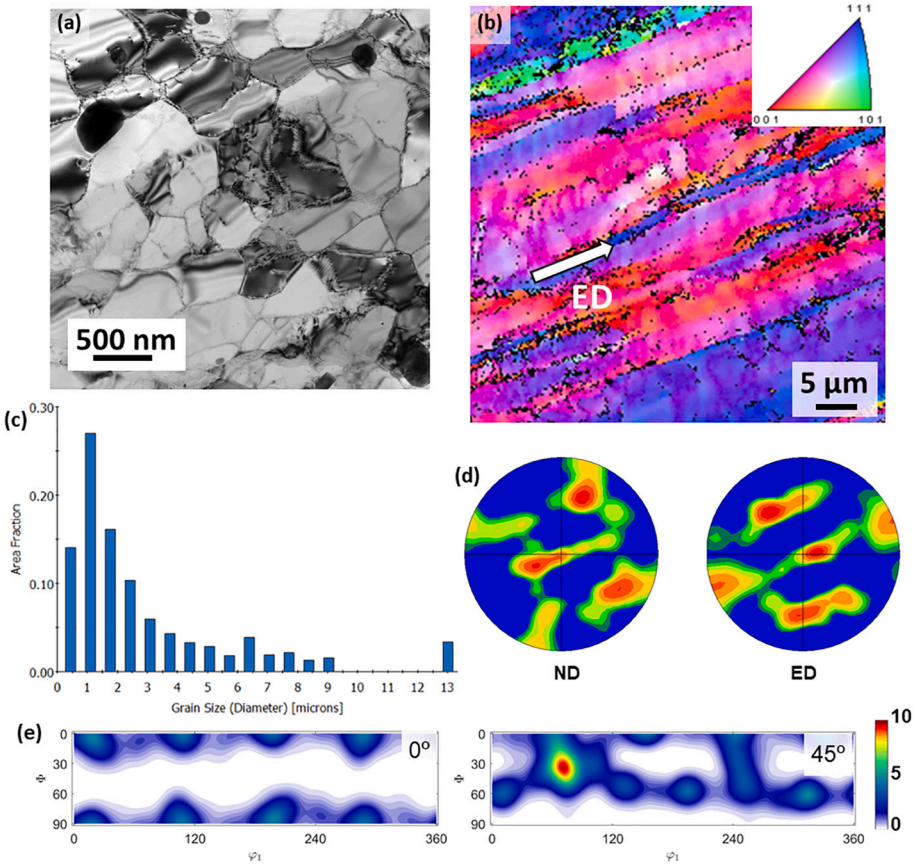

Fig. 2. Pilger processed tubing annealed at 1200 °C (a) TEM image (b) EBSD generated IPF map (c) grain diameter distribution (d) Pole Figures in the ND and ED (e) ODF represented as sections through Euler space at constant φ2 values of 0° and 45°.

mill. The powders were sealed in stainless steel cans, backfilled with Ar, and degassed at 400 °C. The canned powders were then hot extruded at 850 °C into a rod or a bulk plate to consolidate the powder [7,8]. This work evaluates FCRD NFA-1 heat after different processing paths for a bulk plate, along with tubing with a wall thickness of 0.5 mm. The bulk plate material underwent hot extrusion at 850 °C and subsequent cross-rolling at 1000 °C. For the hydrostatically extruded tube the starting ball milled powder was canned and extruded into a rod form at 850 °C. Then thick walled tubes were cut from the extruded rod. The hydrostatic extrusion was applied once with a 4:1 area reduction at 815 °C at Case Western Reserve University. Two other tubes underwent pilger processing after hot extrusion into a rod. For the pilger processed tube at Pacific Northwest National Laboratory (PNNL), the billets were canned in copper and hot extruded to a final thick wall tube through a two-step extrusion process. Following extrusion the thick wall tubes had an inner diameter of approximately 0.200 in. and as extruded outer diameter of 0.375 in.. Sections of the thick wall tube were then processed through a pilger rolling mill. The first tubing was pilger processed 4 times with intermediate anneals at 800 °C for 1 h. Overall reduction of the tubes was 82% from thick wall tube to the final 0.242 in. outer diameter and 0.200 inner diameter tube.

The second tubing was pilger processed with intermediate anneals at 1200 °C at the French Atomic Energy Commission (CEA). The mechanically alloyed powders were encapsulated in a 75 mm diameter soft steel can and degassed at 400 °C. Then the cans are extruded at 850 °C. Subsequently the steel claddings were manufactured using a three-roll type high-precision tube rolling mill. Cold rolling passes and intermediate annealing at 1200 °C were repeated until reaching a 10.73 mm outer diameter.

The microstructures were characterized by TEM and EBSD. 3 mm disks were electro discharge machined (EDM) from the faces of the cladding tubes. The TEM foils were prepared by mechanical polishing followed by jet electropolishing using a solution of perchloric acid (5%) and methanol at −40 °C with an applied voltage of 20 V until perforated.

The TEM studies were carried out on a FEI Tecnai F30 operating at 300 kV. EBSD with automated phase indexing was performed in a FEI Scios™ dual beam scanning electron microscope (SEM)/focused ion beam (FIB) with an EDAX TSL Hikari camera. The EBSD measurements were carried out at 20 kV, current of 1.6 nA, and step size of 0.08–0.18 µm. Samples for EBSD and micro-mechanical testing were mechanically polished to a thickness of ~100 µm, and then electropolished for ~30s to remove surface damage. Grain size, misorientation, and texture were analyzed using the TSL OIM Data Analysis 8 software package. The grain size and aspect ratios were determined from relatively large scans ranging from 45 × 60 µm in the finest grained tubing to 110 × 165 µm in the largest grain tubing, as shown in S1, in the supplementary materials. Higher magnification EBSD maps on the same scale are shown in the following figures. The orientation maps and pole figures are shown with their normal direction (ND) through the page, while the extrusion direction (ED) is perpendicular. Orientation Distribution Function (ODF) were created in MTEX. Points with a confidence index less than 0.05 are displayed as black dots in the inverse pole figure maps shown in this work.

The micropillars were fabricated in a dual beam FEI Scios™ SEM/FIB, using a beam of Ga^+ ions to remove the material and shape it in pillar form. Micro-pillars were fabricated on areas where EBSD maps were collected, therefore the top surface grain size and orientation of the pillars are known. All micro-pillars had height-to-diameter ratio of around 2:1 (20 µm:10 µm) and around six degrees of vertical taper. Due to the taper the diameter measured at the pillar top (the smallest measurement) was used for stress calculations. The engineering stress-strain curves were calculated from the load-displacement data and the 0.2%

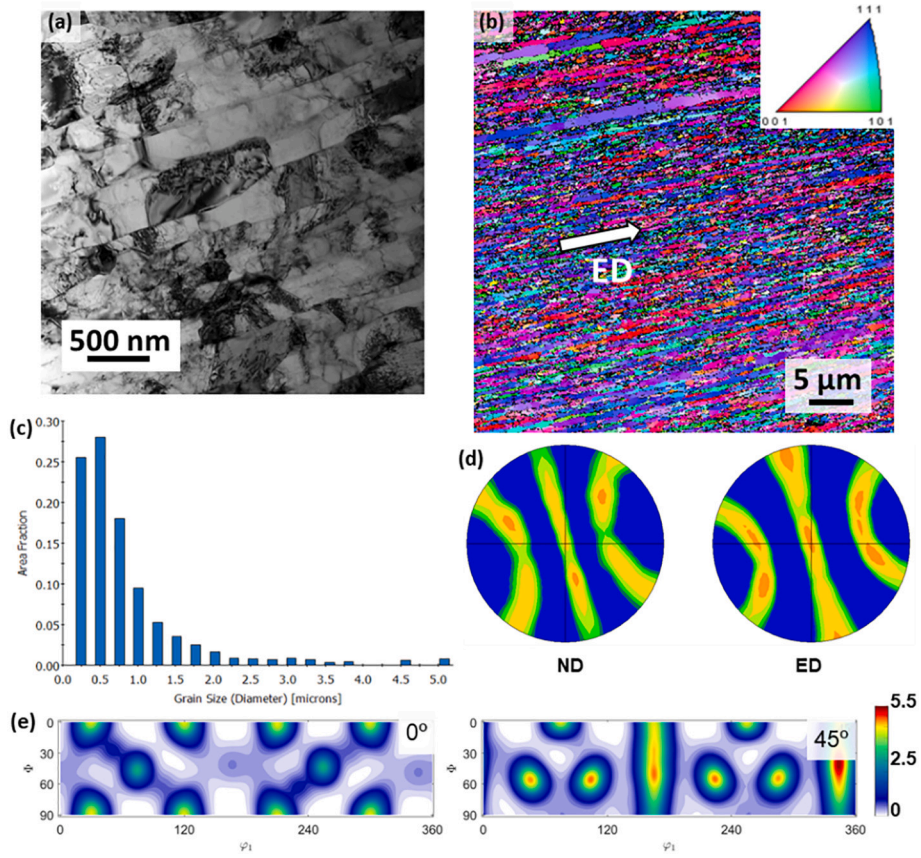

Fig. 3. Hydrostatically extruded tubing at 815 °C (a) TEM image (b) EBSD generated IPF map (c) grain diameter distribution (d) Pole Figures in the ND and ED (e) ODF represented as sections through Euler space at constant φ2 values of 0° and 45°.

offset yield stress was determined. 4–5 pillars of each processing condition were tested in micro-compression. *In-situ* uniaxial compression tests were conducted to capture the local microstructural evolution during the course of deformation [25,26].

The *in-situ* testing was conducted in a nanomechanical instrument, which is comprised of a nano-mechanical tester (Alemnis Indenter system) inside of a SEM (FEI Scios™). The pillars were compressed with a flat punch conductive diamond tip of 20 μm diameter, at a nominal strain rate of 10^{-3}/s. The continuously captured image scans were recorded as a video file during the test.

3. Results and discussion

3.1. Grain structure

Deformation behavior in NFAs is complex and varies with the deformation pathways. Previous work on 14YWT after compression showed that the main texture types are α- and γ -fibers with 001<110> and 111<110> components, which are two of the common rolling textures in bcc metals [27]. All extrusion pathways investigated in this work had elongated grains and the presence of γ -fibers. The development of the γ fiber is also linked to better formability of steels with a high Cr content, enabling the production of these tubes without cracking.

3.1.1. Hot extrusion followed by cross-rolling into a plate

The microstructure generated after hot extrusion at 850 °C and subsequent cross-rolling at 1000 °C was analyzed in the normal direction perpendicular to the extrusion direction. The hot extruded and cross-rolled plate (Fig. 1) displays a bimodal grain distribution with an average diameter of 0.85 μm for the smaller grains and 6.5 μm for the larger grains. Both grain sizes have a similar aspect ratio (d_{min}/d_{max}) of 0.6–1.0. The TEM images and the EBSD inverse pole figure (IPF) maps display similar aspect ratio grains. A preferred ⟨001⟩ crystallographic orientation texture is present. The ODF maps indicate a strong θ fiber along the {001} <110> orientation, as shown in [21]. These bimodal grain sizes align with previous studies showing similar overall <001> texture as well as a majority of small grains <1 μm in diameter and some larger grains >9 μm in diameter [21,24].

3.1.2. Pilger processing with intermediate anneals at 1200 °C

Increasing the annealing temperature to 1200 °C after pilger processing also results in a larger grain size as expected (Fig. 2). A bimodal distribution shows smaller grains with 1.25 μm average diameter and the larger grains with 7.5 μm average diameter, with their aspect ratios ranging from 0.40–0.80. This is the largest grain diameter among all 3 tubing routes studied in this work. The grains either show a ⟨111⟩ or ⟨001⟩ texture, with few intermediate textures. The ODF maps do not reveal a strong fiber texture and a weak ε-fiber is present at {112} < 111>. The development of a {112}⟨111⟩ texture in 14YWT annealed to 1150 °C after deformation has been noted in [28]. Additional studies on pilger processed ODS steels with 1050 °C annealing temperatures have also reported bimodal grain sizes and weaker textures [23]. Furthermore, FeCrAl ODS after pilger processing and recrystallization at 1150 °C exhibited a similar grain aspect ratio and texture, but much larger grain sizes with an average grain size of 98 μm [29].

3.1.3. Hydrostatic extrusion at 815 °C

In comparison, the hydrostatically extruded tube at 815 °C (Fig. 3) displays a stronger <111> overall texture and much smaller, elongated grains. Grains have an average 0.45 μm diameter and an aspect ratio range of 0.15–0.30. These results follow previous microstructural characterization of an NFA hydrostatically extruded tube having <111>

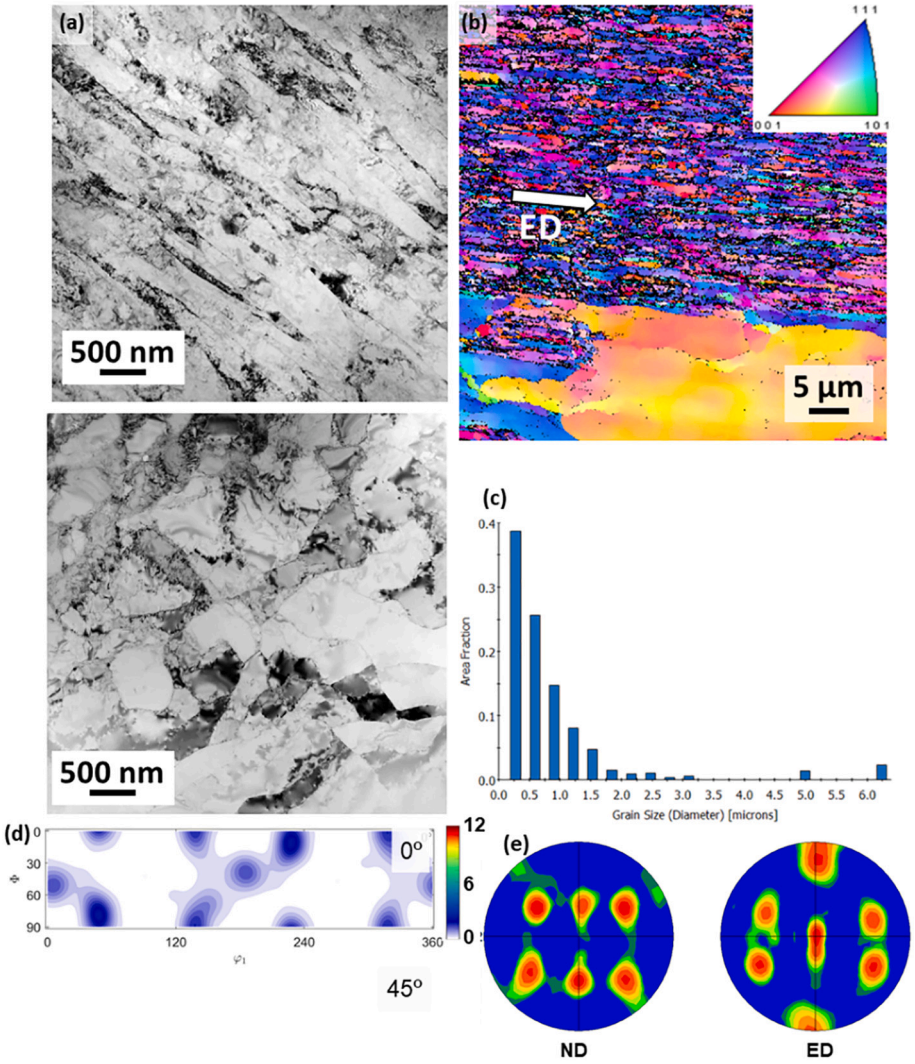

Fig. 4. Pilger processed tubing annealed at 800 °C (a) TEM images (b) EBSD generated IPF map (c) grain diameter distribution (d) Pole Figures in the ND and ED (e) ODF represented as sections through Euler space at constant φ2 values of 0° and 45°.

texture and fine grains with an average 0.49 µm diameter [21]. The presence of an α fiber is found in the ODF maps and the intensity of the orientation is reduced compared to the extruded and rolled plate. A stronger γ -fiber at {111}⟨112⟩ is present, as expected due to conventional texture development in bcc materials, and after deformation the {111}⟨110⟩ texture component expands towards the {111}<112 > component [28]. The main difference between this work and previous reports in literature is the absence of bimodal grain sizes, which may be attributed to differences in processing conditions [21,30]. The hydrostatically extruded tube in this work was first hot extruded into a rod, while previous work first cut a rod cut from a plate and subsequently hydrostatically extruded into a tube. Variation in stress states between these processing routes could have altered the resultant grain size distribution.

3.1.4. *Pilger processing with intermediate anneals at 800 °C*

The pilger processed tube annealed at 800 °C displays bimodal grain sizes as shown in Fig. 4 and the finest grain sizes. Fine grained regions have an average diameter of 0.40 µm and a general <111> texture. Bands of coarse grains have an average diameter of 5.0 µm. The pole figures have a higher intensity than in the other processing paths, indicating the greater degree of anisotropy. TEM images of different regions reveal grains varying aspect ratios, showing a heterogenous distribution of the grain shapes and sizes. As is common in deformed bcc materials, a partial γ -fiber at {111}<110 > is observed. Previous work for pilger processed duplex steel after hot extrusion at 1100 °C also showed a partial γ-fiber in the ferrite phase that developed [27]. Pilger processing of a similar NFA with 12% Cr, extruded at 850 °C, exhibited similar grain sizes and aspect ratios with orientations closer to the (101) direction [31].

In summary, hydrostatic extrusion and pilger processing yielded more intense <111> orientation textures compared to the hot extruded and crossed rolled plates. Annealing at lower temperatures of 800–815 °C (at 815 °C for the hydrostatically extruded tubes, and at 800 °C for the pilger processed alloys) resulted in smaller grain sizes, while higher temperatures of 1000–1200 °C (for alloys generated after hot extrusion at 850 °C and subsequent cross-rolling at 1000 °C, and after pilger processing with intermediate anneals at 1200 °C) produced larger average grain sizes. Most processing pathways resulted in bimodal grain distributions, except for the hydrostatically extruded tube. The differences in grain sizes and orientations is thought to be linked to the stress state experienced during the processing in addition to the NO distribution in the microstructure [15].

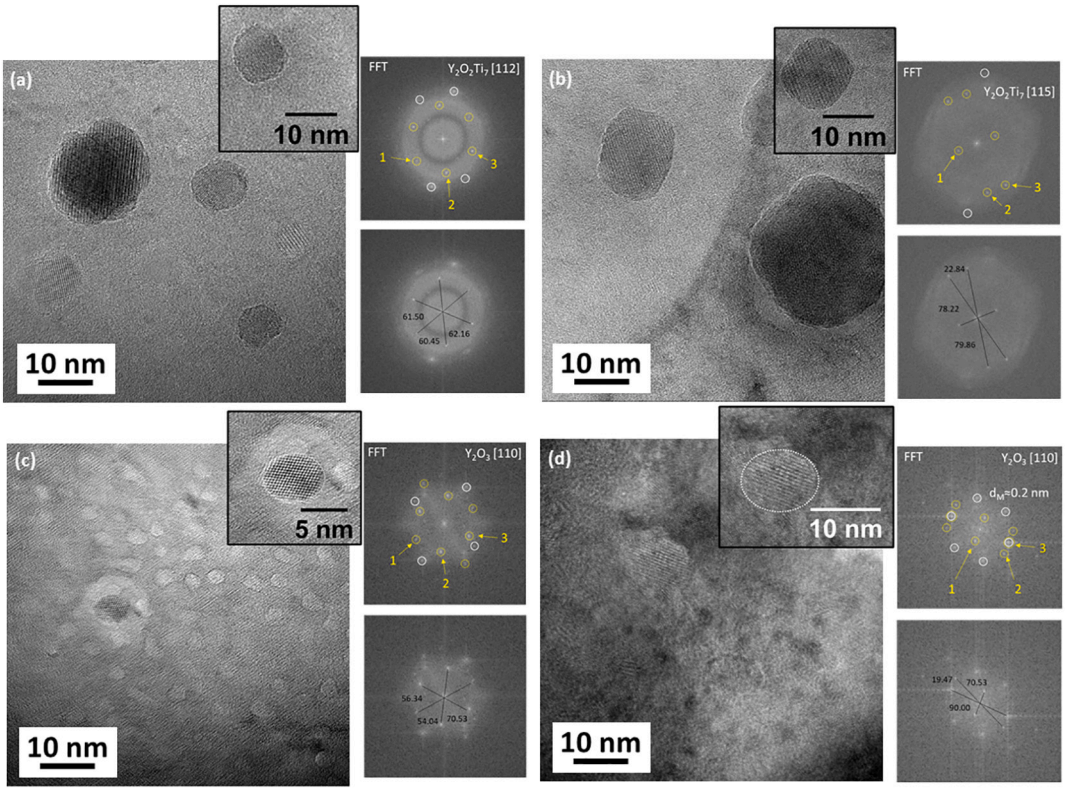

Fig. 5. Representative TEM images with close up images of oxide particles with the corresponding FFTs. In the FFT images, the white circles are from matrix and yellow dotted line circles are oxide particles as analyzed in Table 2. The arrows point to the spot measurement listed in Table 1. (a) Hot extruded at 850 °C and Cross-rolled at 1000 °C, (b) Pilger processed tubing at 1200 °C, (c) Hydrostatic extrusion tubing at 815 °C, (d) Pilger processed tubing at 800 °C. (For interpretation of the references to colour in this figure legend, the reader is referred to the web version of this article.)

Table 1
Measured and theoretical interplanar distances and angles for the particles highlighted in the FFT images in Fig. 5.

		d1 (Å)	d2 (Å)	d3 (Å)	α12 (°)	α13 (°)	α23 (°)
5a		$(\bar{2}\bar{2}2)$	$(\bar{3}11)$	$(\bar{1}3\bar{1})$			
	Measured	0.29	0.30	0.30	60.45	61.50	62.16
	$Y_2Ti_2O_7$-[112]	0.30	0.30	0.29	62.96	58.52	58.52
5b		$(\bar{2}20)$	$(46\bar{2})$	$(64\bar{2})$			
	Measured	0.36	0.14	0.14	79.86	78.22	22.84
	$Y_2Ti_2O_7$-[115]	0.36	0.13	0.13	79.11	79.11	21.79
5c		(004)	$(\bar{2}22)$	$(\bar{2}2\bar{2})$			
	Measured	0.51	0.18	0.20	67.19	88.00	20.80
	Y_2O_3-[011]	0.53	0.18	0.19	70.53	90.00	19.47
5d		(002)	$(\bar{4}42)$	$(\bar{4}40)$			
	Measured	0.26	0.30	0.30	54.04	56.34	69.25
	Y_2O_3-[011]	0.26	0.31	0.31	54.74	54.74	70.53

3.2. Nano-oxide characterization

TEM micrographs show a variation in the oxide particle distribution and structure among the different processing methods. Small, generally rectangular particles ranging from 3 to 9 nm in size to larger more spherical particles ranging from 15 to 24 nm in diameter were observed. Representative TEM images are shown in Fig. 5 for each processing condition. Generally, higher processing temperatures show larger particles in the matrix. The tubing annealed at lower temperatures shows more numerous smaller particles with some larger particles within the matrix. The coherency between the smaller particles and the matrix is greater than the larger particles, as observed in the images. These observations align with previous investigations of 14YWT [30]. Fast Fourier Transform (FFT) of high resolution TEM (HRTEM) of particles was used to determine the oxide structure. The analysis follows that described in [32], where the measured d-spacings and angles from the diffraction spots in the FFT of oxide particles are compared to theoretical values in Table 1.

In the hot extruded plate (Fig. 5a), the FFT indicates the oxide particles of ~9 nm in diameter are $Y_2Ti_2O_7$ along [112] axis. In the pilger processed tube annealed at 1200 °C (Fig. 5b), slightly larger particles of ~10 nm in diameter are more prevalent and are determined to be $Y_2Ti_2O_7$ along [115] axis. The oxides in the hydrostatically extruded tube at 815 °C (Fig. 5b) are smaller in size with an average 5 nm diameter and the identified particles are shown to be Y_2O_3 along the [011] axis. Similarly, the same particles are observed in the pilger processed tubing at 800 °C (Fig. 5d).

Half the identified oxide particles possessed a $Y_2Ti_2O_7$ pyrochlore structure, which has been reported as the typical structure of small oxides in NFAs [32,33]. Other studies employing TEM and atom probe tomography also showed NOs to be Y_2TiO_5 or $Y_2Ti_2O_7$ [34,35]. $Y_2Ti_2O_7$ particles in NFAs were found to be smaller in size than other oxide particles, and generally non-equiaxed and elongated in the deformation direction. Similarly, in the NFA-1 tubing, larger oxide particles are more circular in shape and less elongated than smaller particles. Since some smaller particles were not able to be identified due to overlap with the matrix, we can conclude Y—Ti rich oxide particles and Y oxide particles are present in all processing paths.

3.3. Mechanical properties

Micro-pillar compression of 14YWT following the different processing routes show that the yield strength generally increases with decreasing grain size, representative engineering stress-strain curves are

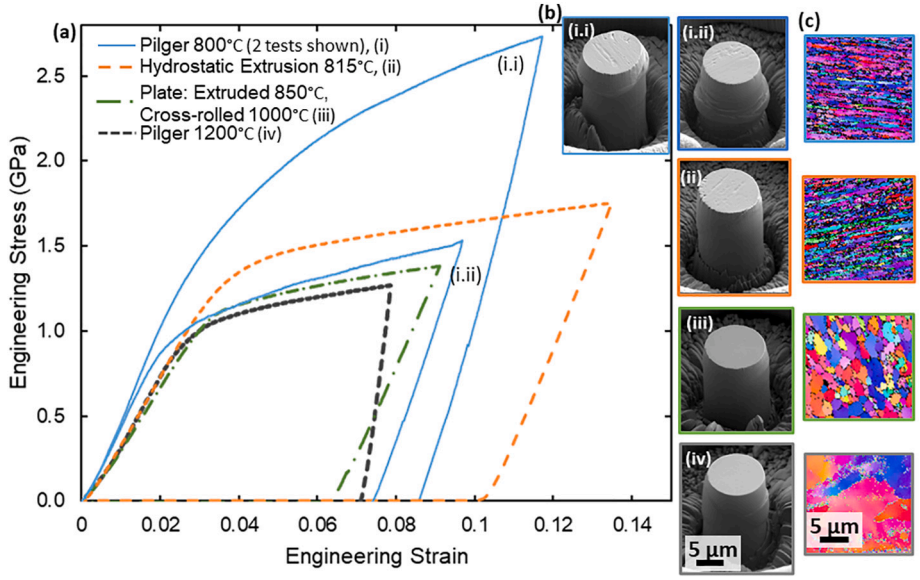

Fig. 6. (a) Micro-pillar compression representative stress-strain curves for each processing path. The pilger processed tube annealed at 800 °C showed a wide range of deformation responses under micro-pillar compression. i.i and i.ii show the higher and lower extremes of these varying responses (see also Fig. S2). (b) SEM images show the corresponding deformed pillars. (c) EBSD IPF maps show the area where the pillars were tested.

Table 2
Summary of microstructure and yield strength of 14YWT after different processing paths. *Bimodal grain size distributions were observed in all paths except in the hydrostatically extruded tubing.

Processing path	Final processing shape	Processing institution	Avg. grain Dia. (μm)		Dominate texture(s)	0.2% yield strength (average ± standard deviation) (GPa)
			<2 μm	>2 μm		
Hot extruded at 850 °C and cross-rolled at 1000 °C	Plate	Los Alamos National Laboratory (LANL)	0.85	6.5	<001>	1.06 ± 0.08
Pilger processed and annealed at 1200 °C	Tubing 0.5 mm wall thickness	French atomic energy commission (CEA)	1.25	7.5	<001>/ <111>	1.01 ± 0.06
Hydrostatic extrusion at 815 °C	Tubing 0.5 mm wall thickness	Case Western Reserve University (CWRU)	0.45*	–	<111>	1.20 ± 0.01
Pilger processed and annealed at 800 °C	Tubing 0.5 mm wall thickness	Pacific Northwest National Laboratory (PNNL)	0.4	5.0	<111>	1.20 ± 0.20

shown in Fig. 6 and the yield strengths are given in Table 2. All engineering stress-strain curves are shown in S2. Thus the plates hot extruded at 850 °C and cross-rolled at 1000 °C, and the pilger processed tubes annealed at 1200 °C with the largest average grain sizes have the lowest average yield strength of 1.06 ± 0.08 GPa and 1.01 ± 0.06 GPa (average ± standard deviation) respectively. In the hydrostatically extruded tubes with significantly smaller grain sizes and a strong <111> texture, the yield strength increases to 1.20 ± 0.01 GPa. These tubes displayed a more homogeneous microstructure with no bimodal grain distribution, leading to less variation between the results. The deformation mode for all 3 pillar types mentioned above was primarily slip-based and generally initiated from the top surface of the pillar (Figs. 6b-ii to 6b-iv).

For all micropillar experiments, the pillar diameter was larger than the grain size in the material, and hence multiple grains are expected to be present within the pillar volume. Thus, while the grain orientation and texture at the top of the pillar surface is known, the texture and grain morphology within the deformed volume is difficult to ascertain. Additionally, three of the processing routes studied in this work have a bimodal grain size distribution (see Table 2). Such heterogeneity could lead to a wide range in the mechanical properties measured in the micro-pillar experiments. This contrasts macro-scale testing where the grain sizes are significantly smaller than the test volume. Therefore, the larger grains within the pillar volume have the potential to influence the overall stress-strain response. This is evident in the tests conducted on the pilger processed tubes annealed at 800 °C, as shown in Fig. 6 and Table 2.

The micro-compression experiments on the pilger processed tubing at 800 °C show a wide variation in their mechanical response, where some pillars experienced a high yield strength of 1.20–1.39 GPa and high strain hardening, and others failed at a much lower yield strength of ~0.9 GPa. This variation is shown in Fig. 6a, which shows the higher (Fig. 6a-i.i) and lower (Fig. 6a-i.ii) extremes of the behavior observed in micro-compression (see also Fig. S2). The post deformation images of the lower yielding pillars in the pilger processed and annealed at 800 °C material also show an unusual bulging at the midsection the pillars (Fig. 6a-i.ii). We speculate that bands of coarse grain regions within the pillar volume, which have lower strengths and hence could have yielded earlier than their finer grained counterparts, are possibly contributing to this unusual deformation behavior and the large variation in properties. Our TEM study (Fig. 5) also indicated that the larger grains possessed a generally lower NO density and the EBSD maps (Figs. 1-4) showed a slightly different texture in the larger grains, both indicating a possible softer behavior in the larger grains upon loading. We note that the other processing conditions with bi-modal grain size distributions (hot extrusion, and pilger processing with intermediate anneals at 1200 °C), and previous micro-pillar compression for ODS steels [36,37], do not show these large variations. A larger statistical study is needed to study

this effect further.

In general, more homogenous microstructures with no bimodal grain sizes in the hydrostatically extruded tube display more uniform yield strength between tests. Our results also match macro-scale tensile tests on a hydrostatically extruded and cross-rolled 14YWT, which have shown yield strengths of 0.97 to 1.1 GPa depending on the orientation [24]. The variation in the macro-scale results was linked to differences in texturing, grain sizes, and microcracks. A similar range in yield strength is observed in this work between the different processing paths and grain sizes. Table 2 summarizes the differences in microstructure, texture, and yield strength of the different processing paths.

One noteworthy observation from Table 2 is that many of the alloys studied in this work have a wide range of grain sizes. Hence the micro-compression experiments in the regions with larger grain sizes could have an overall lower response due to the presence of fewer grain boundaries within the pillar volume. Such bimodal or multi-modal grain size distributions are expected to be detrimental to the bulk properties of these alloys. To effectively determine a bulk material response, larger pillar volumes (possibly using macro-scale testing) are required.

4. Conclusions

This work investigated the effect of different processing paths and annealing temperatures of a specific heat of 14YWT on the resultant microstructure and mechanical properties. Hydrostatic extrusion and pilger processing of 14YWT into thin walled tubing results in a stronger <111> texture in the normal direction with elongated grains in the extrusion direction, as well as the presence of γ -fiber at <110>. Lower annealing temperatures (800–815 °C) show fine grain sizes with average diameters of ~0.4 μm and aspect ratios of 0.15–0.30. However, the pilger processing resulted in bimodal grain sizes with bands of course grains having an average diameter of 6.0 μm. Higher annealing temperatures in pilger processing at 1200 °C led to grain growth to average diameters of 1.25 μm for small grains and 7.5 μm for large grains. The more extreme variation between the fine and coarse grains was observed in the pilger processed tubing at 800 °C, resulted in a large variation of yield strength observed in the micro-pillar compression (0.9–1.4 GPa). In contrast, the hydrostatically extruded tubing at 815 °C exhibited the lowest variation in yield strength of 1.20 ± 0.01 GPa. Processing paths leading to larger grain sizes resulted in lower yield strengths of ~1.05 GPa. Higher processing temperatures also resulted in variation in the oxide particle distribution, decreasing the number of oxides and increasing the size of oxides within the grains. TEM analysis found both $Y_2Ti_2O_7$ and Y_2O_3 nano-oxides present after the different processing paths. In summary, the hydrostatically extruded tube at 815 °C provided the most homogenous microstructure and a tighter spread of mechanical response among the four processing routes studied in this work. The bimodal grain size distribution, and corresponding stress localization, within some of the processing routes is a cause for concern, and needs to be followed up with future macro-scale mechanical testing.

Supplementary data to this article can be found online at https://doi.org/10.1016/j.matchar.2020.110744.

Declaration of Competing Interest

The authors declare that they have no known competing financial interests or personal relationships that could have appeared to influence the work reported in this paper.

The authors declare the following financial interests/personal relationships which may be considered as potential competing interests.

Acknowledgements

This work was partially funded by the Advanced Fuels Campaign in DOE-NE. CH acknowledges support from the DOE Integrated University Program Graduate Fellowship for this work. CH also acknowledges discussions with colleagues at the Swiss Federal Laboratories for Materials Science and Technology (EMPA) in Thun, Switzerland, as well as funding from the ThinkSwiss research scholarship for the micro-mechanical experiments shown in this work. CH and SP acknowledge funding from NSF MRI #1726897, NSF CMMI #1841331 and DOE DE-NE0008739 for this work.

This work was performed, in part, at the Center for Integrated Nanotechnologies, an Office of Science User Facility operated for the U. S. Department of Energy (DOE) Office of Science. Los Alamos National Laboratory, an affirmative action equal opportunity employer, is managed by Triad National Security, LLC, for the National Nuclear Security Administration of the U.S. Department of Energy under contract 89233218CNA000001.

The raw/processed data required to reproduce these findings cannot be shared at this time as the data also forms part of an ongoing study.

References

[1] G.R. Odette, Recent progress in developing and qualifying nanostructured ferritic alloys for advanced fission and fusion applications, J. Mater. 66 (2014) 2427–2441.
[2] G.R. Odette, On the status and prospects for nanostructured ferritic alloys for nuclear fission and fusion application with emphasis on the underlying science, Scr. Mater. 143 (2018) 142–148.
[3] R.L. Klueh, D.J. Alexander, Impact behavior of reduced-activation steels irradiated to 24 dpa, J. Nucl. Mater. 233-237 (1996) 336–341.
[4] G.R. Odette, M.J. Alinger, B.D. Wirth, Recent developments in irradiation-resistant steels, Annu. Rev. Mater. Res. 38 (2008) 471–503.
[5] A.G. Certain, K.G. Field, T.R. Allen, M.K. Miller, J. Bentley, J.T. Busby, Response of nanoclusters in a 9Cr ODS steel to 1dpa, 525°C proton irradiation, J. Nucl. Mater. 407 (2010) 2–9.
[6] E. Aydogan, N. Almirall, G.R. Odette, S.A. Maloy, O. Anderoglu, L. Shao, J. G. Gigax, L. Price, D. Chen, T. Chen, F.A. Garner, Y. Wu, P. Wells, J. J. Lewandowski, D.T. Hoelzer, Stability of nanosized oxides in ferrite under extremely high dose self ion irradiations, J. Nucl. Mater. 486 (2017) 86–95.
[7] M.K. Miller, D.T. Hoelzer, E.A. Kenik, K.F. Russell, Stability of ferritic MA/ODS alloys at high temperatures, Intermetallics 13 (2005) 387–392.
[8] B. Mazumder, C.M. Parish, H. Bei, M.K. Miller, The role of processing route on the microstructure of 14YWT nanostructured ferritic alloy, J. Nucl. Mater. 465 (2015) 204–211.
[9] N. Sallez, C. Hatzoglou, F. Delabrouille, D. Sornin, L. Chaffron, M. Blat-Yrieix, B. Radiguet, P. Pareige, P. Donnadieu, Y. Bréchet, Precipitates and boundaries interaction in ferritic ODS steels, J. Nucl. Mater. 472 (2016) 118–126.
[10] A. Alamo, V. Lambard, X. Averty, M.H. Mathon, Assessment of ODS-14%Cr ferritic alloy for high temperature applications, J. Nucl. Mater. 329-333 (2004) 333–337.
[11] M.J. Alinger, On the Formation and Stability of Nanometer Scale Precipitates in Ferritic Alloys during Processing at High Temperature Service, University of California, Santa Barbara, 2004.
[12] M.J. Alinger, G.R. Odette, G.E. Lucas, Tensile and fracture toughness properties of MA957: implications to the development of nanocomposited ferritic alloys, J. Nucl. Mater. 307-311 (2002) 484–489.
[13] T.S. Chou, H.K.D.H. Bhadeshia, Crystallographic texture in mechanically alloyed oxide dispersion-strengthened MA956 and MA957 steels, Metall. Trans. A. 24 (1993) 773–779.
[14] T.S. Chou, H.K.D.H. Bhadeshia, Dynamic recrystallisation in hot deformed oxide dispersion strengthened MA956 and MA957 steels, Mater. Sci. Technol. 11 (1995) 1129–1138.
[15] X. Boulnat, M. Perez, D. Fabregue, T. Douillard, M.-H. Mathon, Y. de Carlan, Microstructure evolution in nano-reinforced ferritic steel processed by mechanical alloying and spark plasma sintering, Metall. Mater. Trans. A 45 (2013) 1485–1497.
[16] Z. Dapeng, L. Yong, L. Feng, W. Yuren, Z. Liujie, D. Yuhai, ODS ferritic steel engineered with bimodal grain size for high strength and ductility, Mater. Lett. 65 (2011) 1672–1674.
[17] E. Aydogan, E. Martinez, K. March, O. El-Atwani, D.L. Krumwiede, P. Hosemann, T. Saleh, S.A. Maloy, Alpha' formation kinetics and radiation induced segregation in neutron irradiated 14YWT nanostructured ferritic alloys, Sci. Rep. 9 (2019) 8345.
[18] B. Fournier, A. Steckmeyer, A.L. Rouffie, J. Malaplate, J. Garnier, M. Ratti, P. Wident, L. Ziolek, I. Tournie, V. Rabeau, J.M. Gentzbittel, T. Kruml, I. Kuběna, Mechanical behaviour of ferritic ODS steels - temperature dependancy and anisotropy, J. Nucl. Mater. 430 (2012) 142–149.
[19] A. Steckmeyer, V.H. Rodrigo, J.M. Gentzbittel, V. Rabeau, B. Fournier, Tensile anisotropy and creep properties of a Fe–14CrWTi ODS ferritic steel, J. Nucl. Mater. 426 (2012) 182–188.
[20] S. Pal, M.E. Alam, S.A. Maloy, D.T. Hoelzer, G.R. Odette, Texture evolution and microcracking mechanisms in as-extruded and cross-rolled conditions of a 14YWT nanostructured ferritic alloy, Acta Mater. 152 (2018) 338–357.
[21] E. Aydogan, S. Pal, O. Anderoglu, S.A. Maloy, S.C. Vogel, G.R. Odette, J. J. Lewandowski, D.T. Hoelzer, I.E. Anderson, J.R. Rieken, Effect of tube processing methods on the texture and grain boundary characteristics of 14YWT nanostructured ferritic alloys, Mater. Sci. Eng. A 661 (2016) 222–232.

[22] S. Ukai, S. Mizuta, M. Fujiwara, T. Okuda, T. Kobayashi, Development of 9Cr-ODS martensitic steel claddings for fuel pins by means of ferrite to austenite phase transformation, J. Nucl. Sci. Technol. 39 (2002) 778–788.
[23] E. Oñorbe, M. Hernández-Mayoral, A. Morrison, M. Serrano, Study of the microstructure and small punch behavior of a 9Cr ODS tube, Nuclear Mater. Energy 20 (2019) 100698.
[24] M.E. Alam, S. Pal, K. Fields, S.A. Maloy, D.T. Hoelzer, G.R. Odette, Tensile deformation and fracture properties of a 14YWT nanostructured ferritic alloy, Mater. Sci. Eng. A 675 (2016) 437–448.
[25] J.S. Weaver, S. Pathak, A. Reichardt, H.T. Vo, S.A. Maloy, P. Hosemann, N.A. Mara, Spherical nanoindentation of proton irradiated 304 stainless steel: a comparison of small scale mechanical test techniques for measuring irradiation hardening, J. Nucl. Mater. 493 (2017) 368–379.
[26] S. Pathak, N. Velisavljevic, J.K. Baldwin, M. Jain, S. Zheng, N.A. Mara, I. J. Beyerlein, Strong, ductile, and thermally stable bcc-mg Nanolaminates, Sci. Rep. 7 (2017) 8264.
[27] K.S. Ragger, S. Primig, R. Daniel, R. Kaiser, J. Paal, C. Mitterer, B. Buchmayr, Cold pilgering of duplex steel tubes: the response of austenite and ferrite to excessive cold deformation up to high strains, Mater. Charact. 128 (2017) 257–268.
[28] E. Aydogan, O. El-Atwani, S. Takajo, S.C. Vogel, S.A. Maloy, High temperature microstructural stability and recrystallization mechanisms in 14YWT alloys, Acta Mater. 148 (2018) 467–481.
[29] S.M.S. Aghamiri, T. Sowa, S. Ukai, N. Oono, K. Sakamoto, S. Yamashita, Microstructure and texture evolution and ring-tensile properties of recrystallized FeCrAl ODS cladding tubes, Mater. Sci. Eng. A 771 (2020).
[30] E. Aydogan, S.A. Maloy, O. Anderoglu, C. Sun, J.G. Gigax, L. Shao, F.A. Garner, I. E. Anderson, J.J. Lewandowski, Effect of tube processing methods on microstructure, mechanical properties and irradiation response of 14YWT nanostructured ferritic alloys, Acta Mater. 134 (2017) 116–127.
[31] D.T. Hoelzer, C.P. Massey, S.J. Zinkle, D.C. Crawford, K.A. Terrani, Modern nanostructured ferritic alloys: A compelling and viable choice for sodium fast reactor fuel cladding applications, J. Nucl. Mater. 529 (2020).
[32] E. Aydogan, C. Rietema, U. Carvajal-Nunez, S. Vogel, M. Li, S. Maloy, Effect of high-density nanoparticles on recrystallization and texture evolution in ferritic alloys, Crystals 9 (2019).
[33] Y. Wu, J. Ciston, S. Kräemer, N. Bailey, G.R. Odette, P. Hosemann, The crystal structure, orientation relationships and interfaces of the nanoscale oxides in nanostructured ferritic alloys, Acta Mater. 111 (2016) 108–115.
[34] A.J. London, S. Lozano-Perez, S. Santra, S. Amirthapandian, B.K. Panigrahi, C. S. Sundar, C.R.M. Grovenor, Comparison of atom probe tomography and transmission electron microscopy analysis of oxide dispersion strengthened steels, J. Phys. Conf. Ser. 522 (2014) 012028.
[35] D. Bhattacharyya, P. Dickerson, G.R. Odette, S.A. Maloy, A. Misra, M.A. Nastasi, On the structure and chemistry of complex oxide nanofeatures in nanostructured ferritic alloy U14YWT, Philos. Mag. 92 (2012) 2089–2107.
[36] S. Lim, C. Shin, J. Heo, S. Kim, H.-H. Jin, J. Kwon, H. Guim, D. Jang, Micropillar compression study of the influence of size and internal boundary on the strength of HT9 tempered martensitic steel, J. Nucl. Mater. 503 (2018) 263–270.
[37] C. Shin, S. Lim, H.-h. Jin, P. Hosemann, J. Kwon, Development and testing of microcompression for post irradiation characterization of ODS steels, J. Nucl. Mater. 444 (2014) 43–48.